

Optimization of x-ray event screening using ground and in-orbit data for the Resolve instrument onboard the XRISM satellite

Yuto Mochizuki^{a,b,*}, Masahiro Tsujimoto^b, Caroline A. Kilbourne^c, Megan E. Eckart^d, Yoshitaka Ishisaki^e, Yoshiaki Kanemaru^b, Maurice A. Leutenegger^c, Misaki Mizumoto^f, Frederick S. Porter^c, Kosuke Sato^g, Makoto Sawada^h, Shinya Yamada^h

^aGraduate School of Science, The University of Tokyo, Bunkyo-ku, Tokyo, 113-0033 Japan

^bInstitute of Space and Astronautical Science, Japan Aerospace Exploration Agency, Sagami-hara, Kanagawa, 252-5210 Japan

^cNational Aeronautics and Space Administration, Goddard Space Flight Center, Greenbelt, MD 20771, USA

^dLawrence Livermore National Laboratory, Livermore, CA 94550, USA

^eDepartment of Physics, Tokyo Metropolitan University, Hachioji, Tokyo 192-0397, Japan

^fScience Education Research Unit, University of Teacher Education Fukuoka, Munakata, Fukuoka 811-4192, Japan

^gInternational Center for Quantum-field Measurement Systems for Studies of the Universe and Particles, Tsukuba, Ibaraki 305-0801, Japan

^hDepartment of Physics, Rikkyo University, Toshima-ku, Tokyo 171-8501, Japan

Abstract. The XRISM (X-Ray Imaging and Spectroscopy Mission) satellite was successfully launched and put into a low-Earth orbit on September 6, 2023 (UT). The Resolve instrument onboard XRISM hosts an x-ray microcalorimeter detector, which was designed to achieve a high-resolution (≤ 7 eV FWHM at 6 keV), high-throughput, and non-dispersive spectroscopy over a wide energy range. It also excels in a low background with a requirement of $< 2 \times 10^{-3} \text{ s}^{-1} \text{ keV}^{-1}$ (0.3–12.0 keV), which is equivalent to only one background event per spectral bin per 100 ks exposure. Event screening to discriminate x-ray events from background is a key to meeting the requirement. We present the result of the Resolve event screening using data sets recorded on the ground and in orbit based on the heritage of the preceding x-ray microcalorimeter missions, in particular, the Soft X-ray Spectrometer (SXS) onboard ASTRO-H. We optimize and evaluate 19 screening items of three types based on (1) the event pulse shape, (2) relative arrival times among multiple events, and (3) good time intervals. We show that the initial screening, which is applied for science data products in the performance verification phase, reduces the background rate to $1.8 \times 10^{-3} \text{ s}^{-1} \text{ keV}^{-1}$ meeting the requirement. We further evaluate the additional screening utilizing the correlation among some pulse shape properties of x-ray events and show that it further reduces the background rate particularly in the < 2 keV band. Over 0.3–12 keV, the background rate becomes $1.0 \times 10^{-3} \text{ s}^{-1} \text{ keV}^{-1}$.

Keywords: XRISM, Resolve, x-ray microcalorimeter, event screening. *Yuto Mochizuki, mochizuki@ac.jaxa.jp

1 Introduction

The X-Ray Imaging and Spectroscopy Mission (XRISM)¹ was successfully launched on September 6, 2023 (UT) into a low-Earth orbit of an inclination of 31 degrees from JAXA’s Tanegashima Space Center using an H-IIA rocket. One of the scientific instruments is Resolve,² which was designed to achieve high-resolution (~ 7 eV FWHM at 6 keV), high-throughput, non-dispersive spectroscopy over a wide energy range (0.3–12 keV) based on x-ray microcalorimetry. The energy resolution of ~ 4.5 eV at 6 keV was actually achieved in orbit.³ Resolve was developed under an international collaboration between JAXA and NASA, with participation from ESA based on the heritages of the X-Ray Spectrometer (XRS) onboard the ASTRO-E satellite,⁴ XRS2 onboard the the ASTRO-E2 satellite,⁵ and the Soft X-ray Spectrometer (SXS) onboard the ASTRO-H satellite.⁶

The Resolve x-ray microcalorimeter spectrometer excels not only in energy resolution but also in low background. The requirement for the background rate is $< 2 \times 10^{-3} \text{ s}^{-1} \text{ keV}^{-1}$, which is equivalent to only one background event per spectral bin per 100 ks exposure. A background level

significantly lower than this requirement was indeed achieved in orbit with the SXS,⁷ which has almost the same design with Resolve.² A combination of hardware and software was needed. For the hardware, the anti-coincidence detector⁸ worked efficiently to reduce the background rate to 23% by providing a signal that software screening used to remove events caused by cosmic-ray hits.⁷ For the SXS software, in addition to the screening based on the anti-coincidence detector signals, a set of event-screening criteria was developed to discriminate signal events by cosmic x-ray photons from other events of various origins, which we collectively call background events. In total, the combination of the two reduced the SXS background rate to 7.3% of the original rate.⁷ Owing to this low background, a new scientific discovery was made only with 17 events from a supernova remnant N132D with SXS.⁹

The purpose of this paper is to describe the event screening of Resolve and present its optimization and performance using the in-orbit and ground data sets. We follow the screening developed for the SXS,⁷ but some new screening items and algorithms were developed for Resolve. We made assessments of the existing and new items using the data taken with Resolve. Satellite-level screening, such as telemetry loss, availability of star-tracking control, and angular distance from targets, are out of scope for this paper. The methods presented in this paper are the latest at the time of the performance verification phase. Updates in the future will be shared with the community through the documents provided for guest observers.

A larger volume of data is available for event screening in Resolve than in SXS, both in orbit and on the ground. As for the in-orbit data, SXS was lost unexpectedly early only 34 days after launch¹⁰ due to the loss of the spacecraft attitude control in 2016, yielding only 366 ks integration of good background data constructed from Earth occultation times. Resolve has been operated in orbit under 50 mK since October 9, 2023, and longer integration by an order has already been accumulated.¹¹

As for the ground data, Resolve acquired a more complete set of data at the highest level of integration^{1,12,13} compared to SXS,¹⁴ including data in the gate valve (GV) open configuration for low-energy calibration (below 4 keV), a more complete set of exposures in the extended high energy band (up to 25 keV), and exposures with monochromatic x-ray lines at additional line energies (six lines from 4.5–11.9 keV versus two lines from 5.4–8.0 keV). Here, the GV is an aperture door with an x-ray transmissive window¹⁵ to keep the cryostat leak-tight before the launch. A special apparatus was used to open the GV on the ground for low-energy data acquisition. Such data sets are not (yet) available in the in-orbit. Monochromatic x-ray sources and high energy lines above 12 keV are unavailable among celestial sources with sufficiently high fluxes. Data have not yet been taken with the GV open in orbit, as the initial attempts to open it were unsuccessful.¹ These ground data sets are thus unique for developing algorithms for event screening.

The structure of this paper is as follows. In § 2, we provide a brief description of the Resolve instrument to make the paper self-explanatory as much as possible. We focus on the signal processing both in orbit and on the ground. References for the other aspects of the instrument can be found in a review¹⁶ and other contributions in this volume. In § 3, we explain the individual event screening items with a particular emphasis on new assessments made with Resolve using various ground and in-orbit data. Software implementations for these screening items are available online at <https://heasarc.gsfc.nasa.gov/lheasoft/help/rslpipeline.html>. In § 4, we present the performance of the initial screening, which is used for data products in the performance verification phase, to meet the requirement using the in-orbit data. In § 5, we discuss

further additional screening to increase the signal-to-noise ratio to further extend the Resolve use cases toward faint sources. The paper is concluded in § 6.

2 Signal processing

2.1 Detector and analog signal processing in orbit

The x-ray microcalorimeter detector consists of $6 \times 6 = 36$ pixels (pixel 0–35) constituting an array with a side length of 5 mm. The array is situated in the center of a Si frame that fans out the electrical connections to the pixels. Portions of the front and back of the frame are coated with Au to assist in the transport of heat, including, on the back, the portions of the frame between pixels.⁸ One of the read-out channels is connected to a pixel (pixel 12) that is displaced from the array and outside of the aperture and is under constant illumination by a dedicated ^{55}Fe calibration source. One corner pixel of the main array is not read out to accommodate this calibration pixel. Each pixel comprises a HgTe x-ray absorber and a suspended Si thermistor. The energy deposited by photoelectric absorption of x-rays is dissipated into heat, which is conducted to the 50 mK heat sink with a thermal time scale of a few ms.¹⁷

Underneath the substrate of the x-ray microcalorimeter, a Si detector is placed with a side length of 10 mm and a thickness of 0.5 mm that is used as an anti-coincidence detector (anti-co).⁸ Cosmic-ray particles (mostly minimum-ionizing protons) interact with the detectors mainly via ionization losses along their track lengths and are detected both by the anti-co (as charge) and the microcalorimeter (as heat). The anti-co spectrum peaks at 200 keV, while the spectrum of calorimeter events coincident with anti-co events peaks at 6 keV, with these peaks corresponding to the energy deposited by a relativistic proton at normal incidence to the anti-co (0.5 mm thick Si)¹⁸ and a calorimeter absorber (0.0085 mm thick HgTe), respectively. The pulse characteristics of cosmic-ray and X-ray events in the calorimeter are identical, which is why the anti-co is essential for rejection of particle events. The anti-co detector is read out by two readout circuits for redundancy.

Each of the 36 microcalorimeter pixels and two anti-co channels is read out individually using a pair of signal and return lines without multiplexing. The output impedance of each detector circuit is reduced by a Junction Field Effect Transistor (JFET) source-follower operated at 130 K¹⁷ before being transferred from inside to outside of the cryostat via a feed-through. The analog signal is received by the analog electronics called X-ray box (XBOX)¹⁷ placed outside of the cryostat. The XBOX provides the bias voltages to the microcalorimeter and anti-co detectors and processes their output by shaping, amplifying, filtering, and sampling at a rate of $80 \mu\text{s}$ (12.5 kHz) with a bipolar 14 bit depth analog-to-digital converter (ADC). The signal-chain hardware up to this part is provided by NASA.

2.2 Digital signal processing in orbit

The rate of the entire time-series data ($12.5 \text{ kHz} \times 16 \text{ bit} \times 38 \text{ channels}$) is too large to fit into the telemetry bandpass to ground stations. Therefore, a significant data reduction needs to be made in the orbit. Events are detected and their time-series data (we call “pulse” hereafter) are processed. A handful of characteristic values are derived for each event, which are downlinked at five ~ 10 -minute contacts per day.¹⁹ When resources are available in the data recorder and the telemetry bandpass, the pulse data of randomly selected events are downlinked for diagnostic

purposes, which are called pulse records. This data reduction is performed using the onboard digital electronics called the Pulse Shape Processor (PSP) provided by JAXA.²⁰

The digitized time-series data are sent from the XBOX to the PSP, which consists of two identical units (PSP-A and PSP-B). Each unit hosts one Field Programmable Gate Array (FPGA) board and two Central Processing Unit (CPU) boards. One FPGA board processes 18 microcalorimeter and 1 anti-co channel. One CPU board processes 9 microcalorimeter and 1 or 0 anti-co channel by default. The two anti-co channels are readouts of the same set of events. We used data from the A side in the presented analysis. All cross-channel processing, such as vetoes, is done on the ground.

The FPGA board is responsible for calculating the time derivative of the incoming microcalorimeter data (ADC samples) from the XBOX using a box car filter. It triggers event candidates based on a threshold applied to the time derivative. The threshold was changed once in orbit (at 19:50 on October 31, 2023) from 75 to 120 as a precaution before the first attempt to open the GV and has been left at that value. The FPGA board also detects events in the anti-co detector data by applying a threshold in ADC samples and derives characteristic values of individual pulses: (1) the arrival time when the threshold is exceeded, (2) the maximum ADC sample value (PHA), and (3) the number of consecutive intervals between samples exceeding the threshold (DURATION). We recognize events with a minimum PHA of 71 (equivalent to an energy deposition of 30.5 keV at PSP A side) and a minimum DURATION of 2 to be cosmic-ray events.

The CPU board is responsible for detecting secondary pulses overlapping others and deriving characteristic values of each pulse in the microcalorimeter data. One of the values is the event grade, which is based on how an event is isolated in time from the others on the same channel. Events with no preceding pulse in a fixed time are called p(rietary) and the others s(econdary). Events without others within ± 69.92 ms are H(igh) grade, those without others within ± 17.52 ms are M(id) grade, and the rest L(ow) grade. For the H and M grade events, the time series data of a pulse is correlated with templates for better characterization of the energy and arrival time. The template is made for each pixel from the average pulse shape of numerous events from 5.9 keV x-ray photons and noise spectra obtained in the absence of pulses. After the correlation at several shifted times (TICK_SHIFT), characteristic values such as the arrival time and pulse height (PHA; the amplitude of correlation) are derived by interpolation. Here, the TICK_SHIFT is a value that represents the extent to which the template pulse is shifted in time relative to a incoming pulse from the initial value. It is calculated by the PSP and takes integer values ranging from -8 to $+7$ in the unit of a sample ($80 \mu\text{s}$).^{20,21} For L grade events, template fitting is not done and their pulses are characterized similarly to anti-co events based on thresholding. Because of this difference, a systematic offset of arrival time arises among different grades. This is calibrated as a function of incoming x-ray energy for each channel²² and corrected on the ground to $\lesssim 5 \mu\text{s}$.

2.3 Data processing on the ground

The ground processing takes several stages from the level 0 to 3 (L0–L3). The L0 products are raw packet telemetry (RPT) files in the FITS format. The L1 products are generated by the pre-pipeline (PPL) developed by JAXA,²³ in which raw telemetry values are converted to engineering values in the First FITS Files (FFF). The relative arrival time correction is made at this stage. The L2 products are generated by the pipeline (PL) developed by NASA,²⁴ in which the engineering values in the L1 products are converted into physical values based on the calibration data base

(CALDB). The L3 products are for quick-look assessment for scientific purposes such as x-ray images, spectra, and light curves.

Event screening is performed in the PL using the `xpipeline` task for the satellite-wide processing and the `rslpipeline` task for the Resolve-specific processing. The following processing items are performed.

1. The good time intervals based on the South Atlantic Anomaly passages, Earth elevation angles, and others are calculated using the `xafilter` and `ahgtigen` tasks.
2. The time of the recycling operation of the adiabatic demagnetization refrigerator (ADR), the 50-mK cooler, is calculated using the `rslctsfluct` and `rsladrgti` tasks.
3. The time of modulated x-ray source (MXS) illumination is calculated using the `rslmxsgti` task.
4. Gain tracking and correction are performed for each event.
5. Various flags that can be used for potential later screening are assigned to each event using the `rslflagpix` and `rslplsclip` tasks.
6. Cleaned event files are generated for scientific usage using the `ahscreen` task.

3 Types of event screening

The Resolve event screening consists of 19 items in three categories as listed in Table 1. The items in the first category are based on the pulse shape (§ 3.1). Characteristic values and flags are derived in the onboard processing for each pulse, which are used to discriminate signal from background events. Those in the second category are based on the relative arrival times of multiple events arising from various physical processes that produce multiple events in the microcalorimeter and/or the anti-co detector (§ 3.2). Those in the third category are based on the Good Time Intervals (GTI; § 3.3). Time intervals not used for scientific purposes due to the spacecraft and instrument operations are identified and removed.

3.1 Screening based on pulse shape

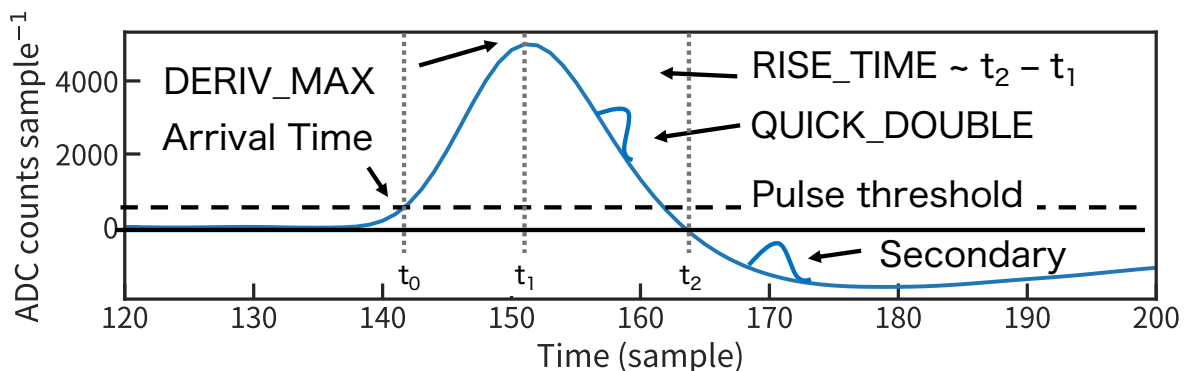


Fig 1 Conceptual example of the time derivative of an event.

The PSP derives several values and flags to characterize individual pulses (Figure 1). `DERIV_MAX` is the maximum value of the time derivative. `RISE_TIME` is defined as the time from the maximum time derivative to the zero-crossing time interpolated for sub-sample resolution. Along with

Table 1 Resolve event screening items.

Item	File ^a	Value ^b	Init scr ^c	Ref
— Screening based on event pulse shape —				
Rise time of a pulse	EVT	RISE_TIME	No	§ 3.1
Time shift in the template fitting	EVT	TICK_SHIFT	Yes	§ 3.1
Maximum of the time derivative of pulse	EVT	DERIV_MAX	No	§ 3.1
Possible overlapping of pulses	EVT	QUICK_DOUBLE	Yes	§ 3.1
Too slow rise or decay times	EVT	SLOW_PULSE ^d	Yes	§ 3.1
Different slope in pulse decay	EVT	SLOPE_DIFFER	Yes	§ 3.1
Possible saturation in the ADC	EVT	FLAG_CLIPPED	No	§ 3.1
— Screening based on relative event timing —				
Veto by the anti-coincidence detector	EVT	STATUS [3]	Yes	§ 3.2.1
“Short” electrical cross-talk	EVT	STATUS [7 : 8]	No	§ 3.2.2
“Long” electrical cross-talk	EVT	STATUS [13 : 14]	No	§ 3.2.3
Frame events	EVT	STATUS [4]	No	§ 3.2.4
Electron recoil events	EVT	STATUS [6]	Yes	§ 3.2.5
— Screening based on time intervals —				
Recycling operation of the ADR	HK	ADRC_CTL_ (CTL MON) _FLUC	Yes	§ 3.3.1
Calibration x-ray illumination (MXS)	EVT	STATUS [9 : 12]	Yes	§ 3.3.2
Calibration x-ray illumination (FW ⁵⁵ Fe)	HK	FW_POSITION1 / 2	Yes	§ 3.3.2
Lost time due to the overload of the onboard CPU	EVT	STATUS [2]	Yes	§ 3.3.3
Passage through the South Atlantic Anomaly	EHK	SAA_SXS	Yes	§ 3.3.4
Occultation by the Earth	EHK	ELV	Yes	§ 3.3.5
Cut-off rigidity	EHK	CORTIME	No	§ 3.3.6

^a Files where the screening information is available (EVT for event files, HK for house-keeping telemetry files, and EHK for the extended HK files).

^b Values used for screening.

^c Whether the item is included in the initial screening.

^d The most significant bit of RISE_TIME is used for this flag.

TICK_SHIFT, PHA, and arrival times (§ 2.2), they are characteristic values of pulses. The maximum and minimum values of TICK_SHIFT are used to indicate that the template fitting was not successful. Events with such values are screened. Other than this, the event properties are not used for the initial screening.

Flags are also given to indicate anomalies in the pulse shape (Figure 2). The QUICK_DOUBLE flag indicates an increase of the time derivative during the decay phase before the trigger threshold is crossed again, which corresponds to the rising edge of the original pulse. SLOW_PULSE and SLOPE_DIFFER flags are set for abnormal rise or slow time scales of primary and secondary pulses, respectively.²⁰ Events with any of these flags are removed, except for events flagged with SLOPE_DIFFER that have $PI > 22000$. Many normal x-ray events at high energy ($E > 11$ keV) receive the SLOPE_DIFFER flag, and these events should not be removed. We examined pulse records of many events with QUICK_DOUBLE, SLOW_PULSE, and SLOPE_DIFFER flags found that they indeed exhibit abnormal pulse shapes.

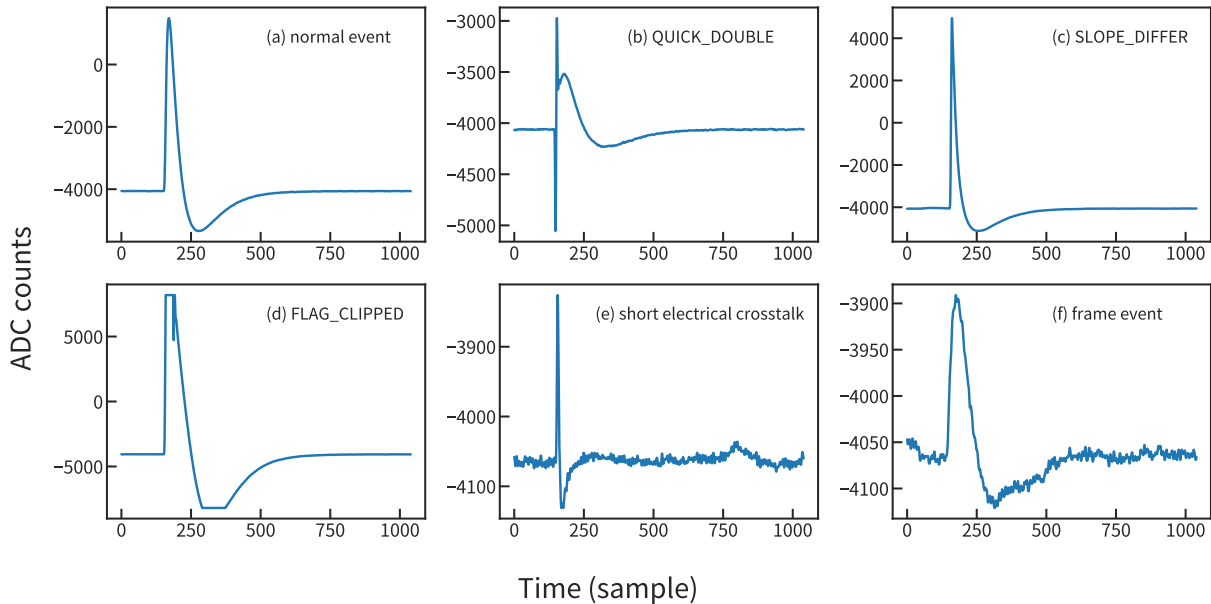


Fig 2 Some examples of the pulse record of (a) normal events and events with (b) QUICK_DOUBLE, (c) SLOPE_DIFFER, (d) FLAG_CLIPPED, (e) short electrical crosstalk, and (f) frame event flags. Examples in (b)–(f) are not intended to be typical.

The FLAG_CLIPPED flag is set for events with a possibility of hitting the maximum of the ADC. Such a flag could be given during the onboard processing when the entire pulse shape is available, but this function was not implemented. In Resolve, the `rs1plsclip` task was developed to flag events of possible ADC saturation based on the pulse height.²⁵ We examined the algorithm using the ground data set taken from February 14, 2022, at 14:05 to February 16, 2022, at 08:40 using a rotating target source, in which targets of an x-ray generator rotate to provide multiple lines over a wide range of energy in the integrated spectra in all event grades.¹² Figure 3 shows the result, in which most FLAG_CLIPPED events appear at energies above 20 keV. Note that the maximum energy before clipping depends on pixel and detector heatsink temperature. Such events are found to degrade the energy resolution at 22 keV. The reason for this change (for high and mid grade events) is because the shape of the gain scale is significantly affected by the pulse clipping

and not accounted for using the standard gain correction techniques. This is not, however, included in the initial screening. Many clipped events are background, from cosmic rays with long tracks in the absorbers, but some may be signals, hence should be included with appropriate screening and redistribution matrix functions in the future.

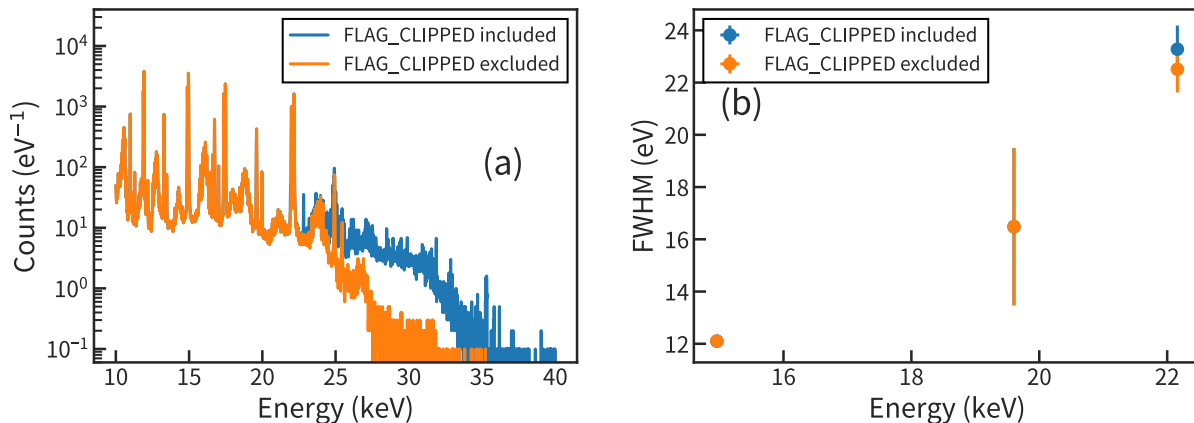


Fig 3 (a) Spectrum after initial screening with and without the `FLAG_CLIPPED` flag. (b) The energy resolution with and without events of `FLAG_CLIPPED` flag using the $\text{Y K}\alpha^1$ (15.0 keV), $\text{Mo K}\beta^1$ (19.6 keV), and $\text{Ag K}\alpha^1$ (22.2 keV) lines. The results are almost identical for the first two lines.

3.2 Screening based on relative timing of multiple events

3.2.1 Anti-coincidence window

We assessed whether the anti-coincidence window used for the SXS also works for Resolve using its in-orbit data. Figure 4 shows the relative timing between the anti-co and microcalorimeter events during times of no ADR recycle (§ 3.3.1), no calibration x-ray illumination (§ 3.3.2), no SAA passages (§ 3.3.4), and the night Earth elevation less than -5 degrees (§ 3.3.5). For the microcalorimeter events, we applied the initial screening (§ 4) except for the anti-co screening, further applied the frame event screening (§ 3.2), and extracted Hp (high primary) grade (§ 2.2) events. The arrival time of anti-co events is earlier than the corresponding Hp microcalorimeter events by -1.860 ± 0.004 and -1.859 ± 0.004 samples respectively for the microcalorimeter event threshold of 75 and 120. The offset between Hp microcalorimeter and anti-co events is caused by their different definition of arrival times (§ 2.2). This is not corrected in the pipeline processing. Instead, the anti-co window is currently set wide enough to encompass the offset (6.25 ± 6.25 samples). This is too wide for the distribution and a narrower window (2 ± 3 samples) would be sufficient.

3.2.2 "Short" electrical cross-talk

Electrical cross-talk is an event for which a fraction of the signal power in a readout line is transferred to the neighboring lines via capacitive coupling. This is considered to happen in the high-impedance part of the readout in the cold stage between the detector and the JFET. The pixel numbering of the microcalorimeter detector is based on the line layout of this part, thus an event in pixel i crosstalks to pixel $i - 1$ and $i + 1$ except for boundaries. Anti-co channels also crosstalk

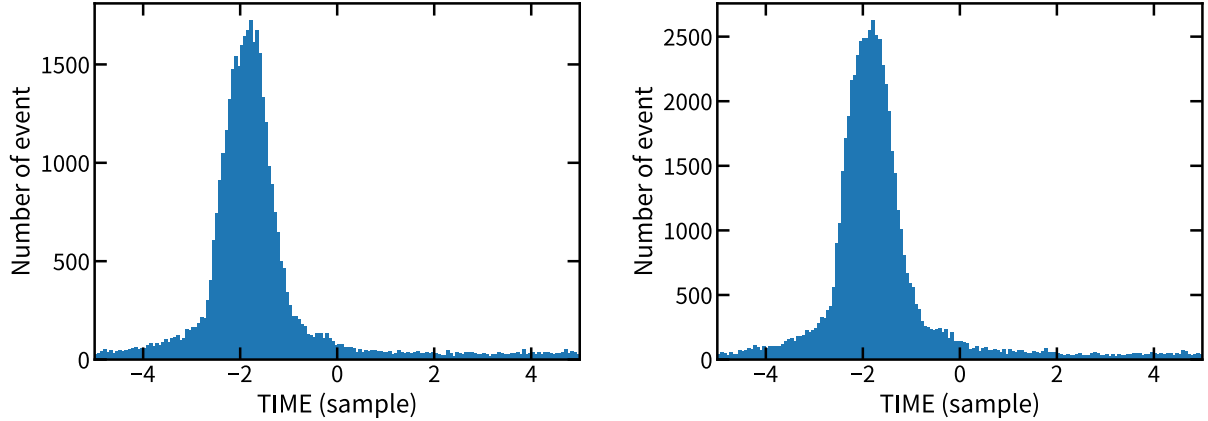


Fig 4 Arrival time of anti-co events relative to microcalorimeter events before (left) and after (right) the change of the event threshold on October 31, 2023. One sample time corresponds to $80 \mu\text{s}$. The offsets for the different event thresholds agree with each other in the range of errors because the use of correlation with the template eliminates dependence of the arrival time on threshold. different thresholds.

to neighboring microcalorimeter channels and vice versa. We call the original events parents and the crosstalk events children hereafter.

Table 2 Data set used for the assessment of “short” cross-talk screening.

Label	Start time	Stop time	Line	Energy (keV)
097091610	2022/02/01 04:00	2022/02/01 08:00	Fe $K\alpha$	6.4
097091650	2022/02/01 20:00	2022/02/02 00:00	Au $L\alpha$	9.7
097091750	2022/02/02 20:00	2022/02/03 00:00	Au $L\beta$	11.4

Child events need to be removed as background, while parent events need to be left as signals. “Short” crosstalk screening refers to the screening when the child events are detected as events above the event threshold. “Long” crosstalk screening refers to screening events contaminated by crosstalk that did not trigger but is inferred. For the short cross-talk screening, we can utilize the relative timing and pulse height between parent-child pairs in neighboring pixels. To better characterize the relation, we used the data of monochromatic x-ray injection of a sufficiently high energy²⁶ so that child events are detected. Three data sets of Fe $K\alpha$ (6.4 keV), Au $L\alpha$ (9.7 keV), and Au $L\beta$ (11.4 keV) lines were used (Table 2). The Fe $K\alpha$ data represents the lowest parent energy for which some child events can trigger for a threshold of 75. The Au $L\beta$ represents the highest end of the required energy band.

Hp events in the energy range of ± 1 keV of the injected line energy were considered parents. Child event candidates for each parent were extracted in two neighboring pixels within a time window and having an energy less than 0.15 keV. Figure 5 and Figure 6 show the result using the Au $L\alpha$ line as an example. Both the relative arrival time and the pulse height ratio have characteristic distributions. For the former, child events precede their parent events by ~ 5 samples. This is reasonable as the child events are faster than their parents due to their capacitive-coupling origin. For the latter, the ratio is typically below 0.005. We made the same assessment for the other two data sets and concluded that the relative window of 2–9 samples and the ratio below 0.005 encompasses the parent-child pairs. This screening is effective for removing background

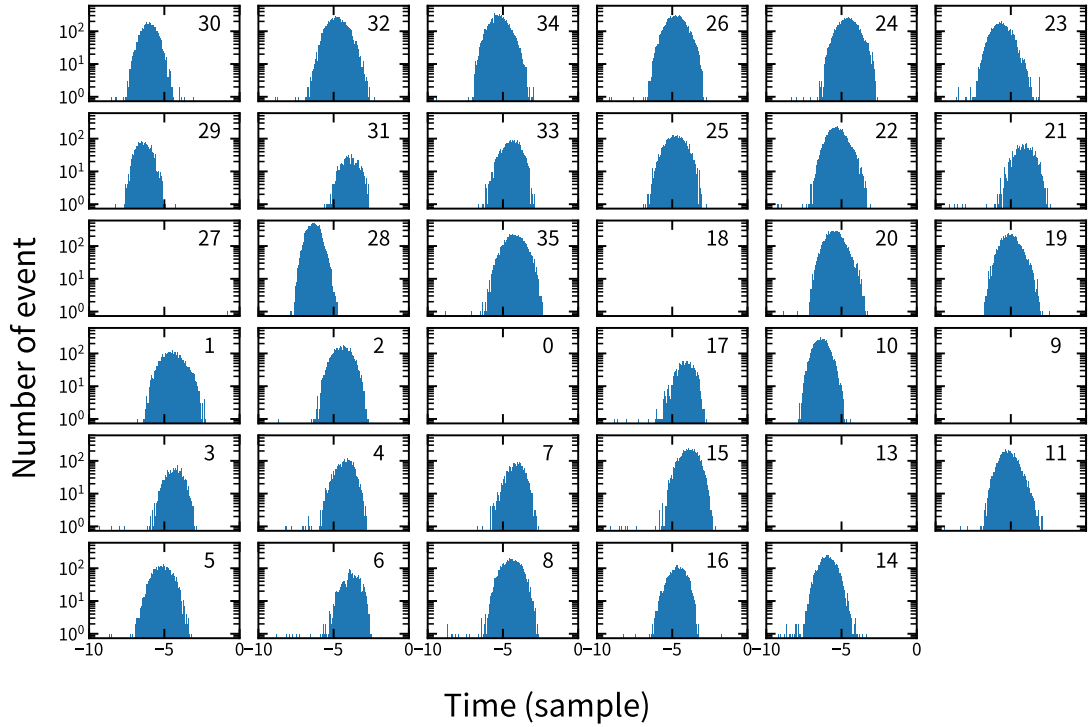
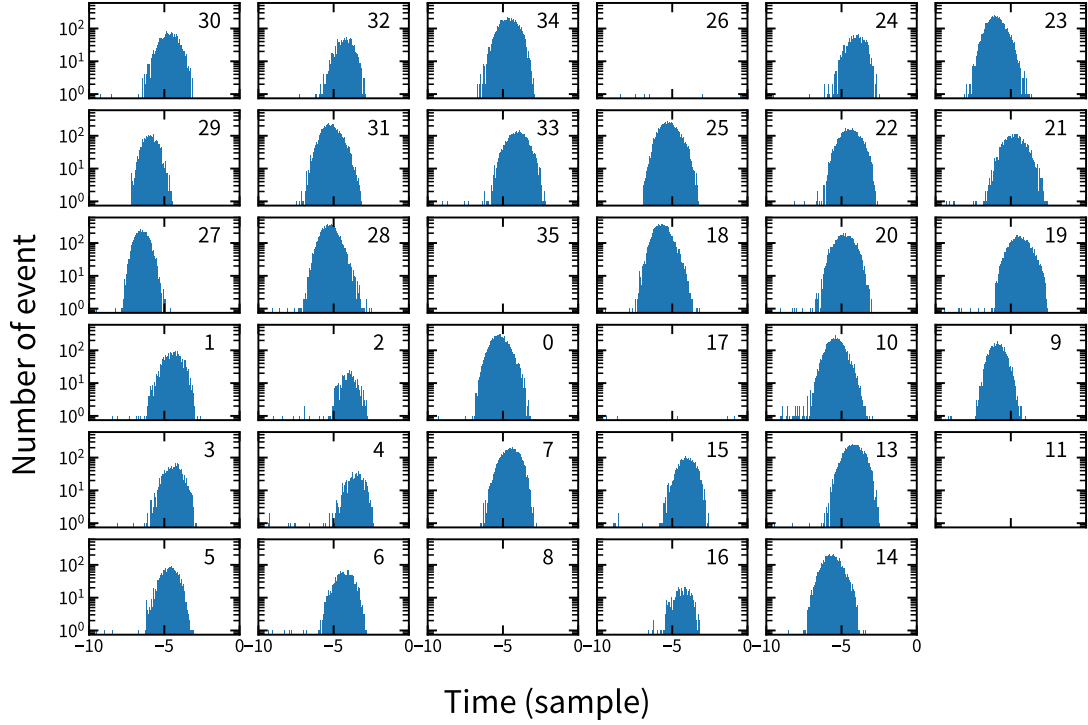


Fig 5 Result of short cross-talk assessment using the Au $L\alpha$ line data of individual pixels, arranged according to the physical layout of the pixels in the array, except for pixel 12 (calibration pixel). The distribution of arrival times of child events in pixel i relative to their parents in pixel $i + 1$ (top) and $i - 1$ (bottom). The child events in pixels $9n + 8$ ($n = 0, 1, 2, 3$) do not have parents in pixel $i + 1$ and child events in pixels $9n$ do not have parents in pixel $i - 1$ due to the boundaries of the readout line layout, which is confirmed with the data with a few false coincidence exceptions

below ~ 0.3 keV, which is relevant only after the GV is opened. Thus, the short crosstalk flags STATUS [7 : 8] are assigned but not used as a part of the initial screening.

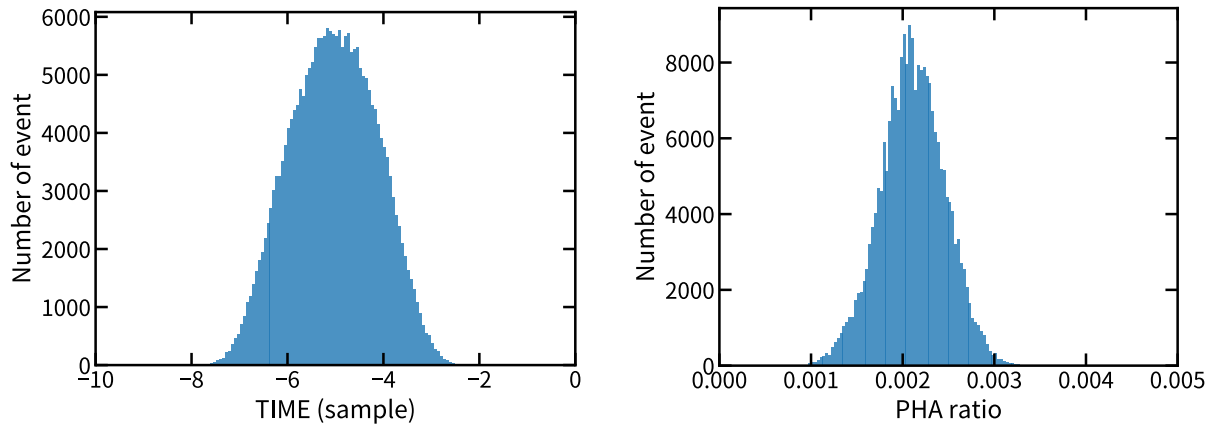


Fig 6 Result of short cross-talk assessment using the Au $L\alpha$ line data of all pixels except for pixel 12 (calibration pixel); (left) arrival time of child event candidates relative to their parents and (right) ratio of the pulse height of child events against parents. We used Hp grade only both for the parent and child events.

3.2.3 “Long” electrical cross-talk

Long cross-talk screening is used to flag events in neighboring pixels that are likely contaminated by crosstalk from each other, resulting in an error in the absolute energy assigned to each pulse. The magnitude and polarity of the error in energy assignment depends on how the crosstalk interacts with the template used to process the event and thus on the offset of the pulses with respect to each other. It also depends on the energy of the neighbor pulse and the coupling between the channels, which is not the same for all neighboring pairs. For bright sources and hard spectra, the accumulated errors have a non-negligible effect compared with the required energy resolution. The optimal screening is currently under development. Careful trade-off studies depending on science cases are needed.

Since the impact is causal, if the shapes of all the crosstalk pulses as a function of energy were known, we could calculate the interaction with the template as a function of offset and correct for it. We may not need to know these pulse shapes very well to significantly reduce the error, but more work is needed.

3.2.4 Frame events

Frame events are caused by cosmic rays hitting the detector frame made of silicon. The dissipated energy propagates as heat to the microcalorimeter pixels, which can detect the disturbance as events if the trigger threshold is exceeded. These events are the predominant background below ~ 2 keV and should be discarded. Frame events exhibit two distinctive characteristics because of their mechanism: (1) Multiple events are detected within a short time period and (2) the detected events have a slow rise time. Based on the first characteristics, we set the window to be ± 9 samples.⁷ to flag the frame event candidates (STATUS [4]). This screening, however, is based only on time coincidence, hence is prone to false coincidence particularly in observations of bright sources. Therefore, this is not currently included in the initial screening.

3.2.5 Electron recoil

An electron recoil event occurs when one of the electrons generated by an incoming x-ray escapes from a pixel and deposits energy in a different pixel. Two events are recorded and the original energy is reconstructed by summing the energy of the two. This screening is possible only for pixel 12, for which the energy of x-ray photons is limited mostly to 5.9 keV (Mn $K\alpha$) or 6.4 keV (Mn $K\beta$). Recoil events between other pixels are removed by the same screening that removes the frame events. The recoil events are distinguished by three criteria; (i) They occur in pixels other than pixel 12, (ii) The sum of the energies of the recoil event and the corresponding event in pixel 12 is less than the energy of Mn $K\beta$ (6.5 keV, including margin), and (iii) the difference of arrival times between the recoil and the original events is within ± 3 samples. A flag is set for recoil events (STATUS [6]), which are removed in the initial screening.

3.3 Screening based on time intervals

3.3.1 ADR recycle

The working temperature for the heat sink of the microcalorimeter array is maintained at 50 mK using the ADR²⁷ and its controller, the ADRC. Two ADRs are used in a series from the 1.2 K interface provided by the depressurized superliquid helium.²⁸ The magnet current runs out in ~ 2 days, and recycling takes ~ 1 hour. Time intervals during the recycling operation need to be removed. The duration is based on the control parameters and on the temperature fluctuations measured by a thermometer placed at the 50 mK stage.²⁹ The algorithm was developed and verified anew for Resolve, and is implemented in the `rsladrgti` task for the initial screening. We confirmed that the new algorithm works by examining many ADR recycles both on the ground and in orbit executed in various conditions.

3.3.2 Calibration x-ray illumination

Resolve has two types of calibration sources for tracking drifts in the energy scales of individual pixels besides the ^{55}Fe calibration source constantly illuminating pixel 12 for tracking variations in common-mode gain.³ One is the modulated x-ray source (MXS),³⁰⁻³² in which the calibration x-rays can be switched on and off at 1/8 ms at the shortest by controlling the light emitting diode for the source of photoelectrons in the x-ray generator.³³ Events during the illumination intervals are distinguished by a set of flags (STATUS [9 : 12]). The other is the ^{55}Fe sources placed in one of the filter wheel (FW) positions.^{30,31} The wheel is rotated during observations to provide intermittent x-ray illumination. Intervals of illumination are distinguished by the wheel position in the HK telemetry (FW_POSITION). Both the MXS and FW are provided by SRON. During the closed GV configuration, we use the filter wheel ^{55}Fe sources for the main calibration source, as they can illuminate the entire array, unlike the MXS.

3.3.3 Pixel lost time

Due to the limited CPU resources onboard, all events are not processed at count rates higher than $\sim 200 \text{ s}^{-1}$. In such a case, the buffer storing events detected by the FPGA is discarded all together, and only the intervals of lost events are downlinked. Each pixel has its own event buffer and each CPU processes nine pixels in a round-robin manner. Therefore, the lost times occur differently among pixels. In most cases, this happens when observing bright point-like sources and pixels at

the array center suffer the largest loss due to the CPU limit. The detailed assessment is described separately.¹³

3.3.4 SAA passage

XRISM passes through the South Atlantic Anomaly (SAA) 8–9 times lasting for 3–30 minutes each in a day of 15–16 rotations around the Earth. Resolve continues to operate in observation mode during the SAA passages and events are collected, which need to be removed based on the position of the spacecraft at the event time.

As the SAA region changes gradually and has shifted westward significantly from the ASTRO-H days, we redefined the region on the two-dimensional longitude–latitude projection based on the in-orbit data of the anti-co detector. Figure 7 shows the anti-co count rate in a 1 s bin averaged over a 2×2 degree grid. We used all the events taken from October 11, 2023, to December 6, 2023. We further removed events in the time intervals of the ADR recycles (§ 3.3.1), x-ray illumination (§ 3.3.2), and night earth elevation larger than -5 degrees. Figure 7 shows the non-x-ray background (NXB) count rate of the array pixels and the energy resolution of pixel 12 as a function of the anti-co count rate. As the count rate increases, the NXB rate increases and the resolution degrades. We set the anti-co rate threshold to be $< 3 \text{ s}^{-1}$. We defined the SAA region (red border in Figure 7) so that all the grids exceeding the threshold are enclosed.

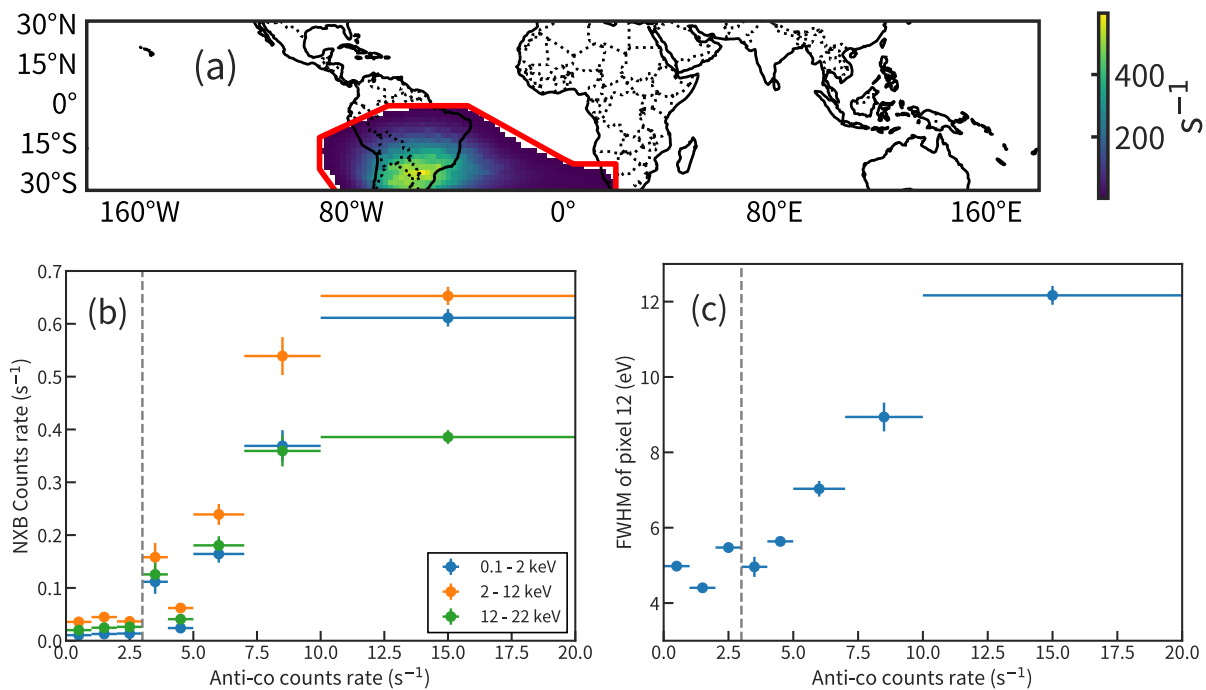


Fig 7 (a) Map of anti-co count rate averaged over a 2×2 degree grid and red border defining SAA region (b) The NXB count rate (all event grades) of all pixels except for pixel 11, 12, and 13 (calibration pixel and its cross-talk neighbors). The rates in three different energy bands are shown in different colors. (c) The energy resolution in eV FWHM of the Mn $K\alpha$ line of pixel 12. Gray dash line in (b) and (c) shows the anti-co threshold used in the initial screening.

3.3.5 Earth occultation

The time intervals when the observed source is occulted by the Earth are removed based on the elevation angle of the source from the Earth limb. We inspected the background rate of the in-orbit data and set the threshold to be >5 degrees for science observations and <-5 degrees for NXB data collection, which are the same as used for SXS. The threshold can be set differently for the Sun-lit Earth (day-Earth elevation) and the Sun-unlit Earth (night-Earth elevation): the former may require a more stringent criteria to avoid Earth albedo in the soft x-ray band. However, because of the closed GV configuration, we see no difference between day and night Earth elevation, except when large solar flares produce significant hard x-ray flux. This will be revisited when the GV is successfully opened.

3.3.6 Magnetic cut-off rigidity

The magnetic cut-off rigidity (COR) is a metric describing the strength of the Earth magnetic field at the moving position of the satellite. When the COR is larger, the cosmic-ray rate is reduced. The NXB rate and the energy resolution degradation depend on COR only weakly,⁷ thus this metric is not used for event screening purposes. Instead, the history of COR during an observation is used to construct the background spectrum dedicated for the observation using the `rslnxbgen` task. The verification of the task is underway as of this writing.

4 Initial event screening

Here, the initial screening is the screening applied for the pipeline products for the performance verification phase. The screening can be applied to all events independently of the observed source. The screening is expected to be more sophisticated as we gain more knowledge or conditions change in the future. A combination of several screening items (Table 1) are used for the initial screening. We now evaluate the performance of the initial screening using the NXB data. Here, the NXB data are constructed using all the data from October 11, 2023 when the 50 mK control started to February 6, 2024 when the commissioning phase was concluded. We merged data both before and after the change of the event threshold to increase the statistics after confirming that the evaluation does not differ between the two. The initial screening for NXB is applied (Table 3). Time intervals of x-ray illumination were also removed. A total exposure time of 650 ks was obtained. The resultant NXB spectrum is shown in Figure 8. The count rate in the 0.3–12 keV band is $1.8 \times 10^{-3} \text{ s}^{-1} \text{ keV}^{-1}$. We conclude that the initial screening is sufficient to meet the requirement of $<2.0 \times 10^{-3} \text{ s}^{-1} \text{ keV}^{-1}$.

5 Additional event screening

5.1 Screening criteria

Although the initial screening in the current pipeline processing is sufficient to satisfy the requirement (§ 4), additional screening, such as applied to the ASTRO-H SXS data, but optimized for Resolve, is expected to improve the signal-to-noise ratio and extend the Resolve capability for specific sources. We exploit the fact that the characteristic values, not flags, of events (i.e.; `DERIV_MAX`, `RISE_TIME`, and `TICK_SHIFT`) are tightly correlated with each other for x-ray events but not for background. For example, the higher the energy deposited, the greater the drop in the resistance of the thermistor, and the resulting change in the electrical component of the signal response time

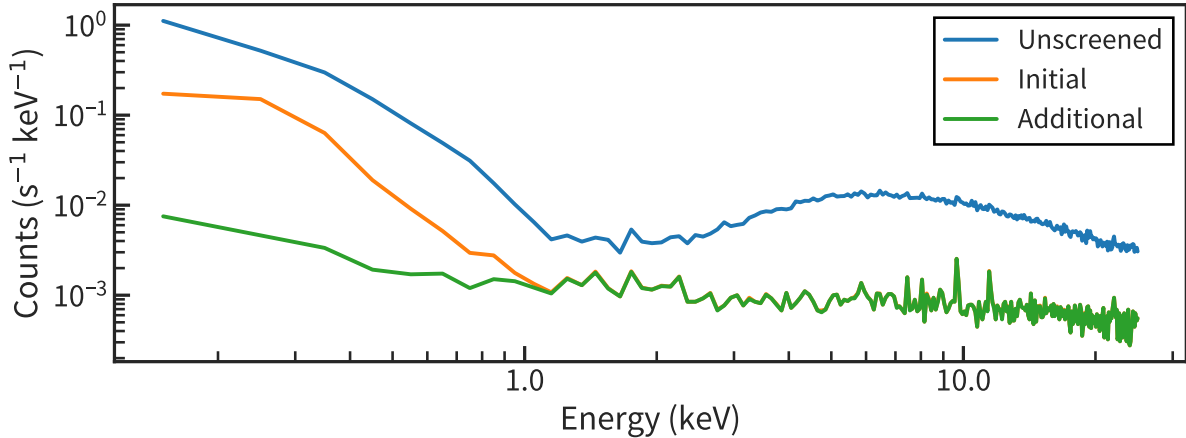


Fig 8 NXB spectra before any event screening (blue), initial screening (orange), and additional screening (green). Events of the Hp and Mp grade are used.

leads to a correlation between `DERIV_MAX` and `RISE_TIME`. Events deviating from this correlation should be considered as background events. Here, we used `DERIV_MAX` as opposed to another proxy of energy used in the previous work,⁷ as the correlation is more linear between `DERIV_MAX` and `RISE_TIME`. Other criteria such as frame (§ 3.2.4) and cross-talk (§ 3.2.2, 3.2.3) events are expected to improve screening further, but they are not presented in this work as they are currently under study.

Figure 9 shows the two-dimensional distribution of Hp and Mp events using the in-orbit data of LMC X-3 observed in late November and early December, 2023. The gray dots indicate events after the initial screening. The correlations among the x-ray events are evident as the main single sequence. The distributions deviating from the main sequence are mostly made with background events, which is confirmed by inspecting the pulse shapes when the pulse record data are available. An exception is the distribution deviating upward from the main sequence at the largest `DERIV_MAX` end, which is made by x-ray events that are clipped. These events may be signals, hence should not be removed. Only for the purpose of clarifying the main sequence, we applied the frame-event screening (§ 3.2.4), which efficiently eliminates many background events though with false coincidence. Based on the frame-screened distribution of events (black dots), we defined the screening criteria shown in blue lines. Note that the presented screening applies for the data taken with the event threshold of 120. `TICK_SHIFT` depends on the trigger threshold, thus different criteria for `TICK_SHIFT` were developed for the data taken with the event threshold of 75.

5.2 Evaluation

We now evaluate the performance of the additional screening. The result of screening depends on the count rate of the celestial object; the background may be reduced further but at a sacrifice of data due to false coincidence. There may be some pixel dependence. For the assessment, therefore, we used the data sets of different origins (Table 3), which include the ground data with the GV open (GVO) and the in-orbit data of Abell 2319 and LMC X-3 observations and NXB data.

Abell 2319 is a galaxy cluster and is a diffuse source with a uniform distribution of events over the microcalorimeter array.³⁴ LMC X-3 is a blackhole binary in the Large Magellanic Cloud³⁵ and

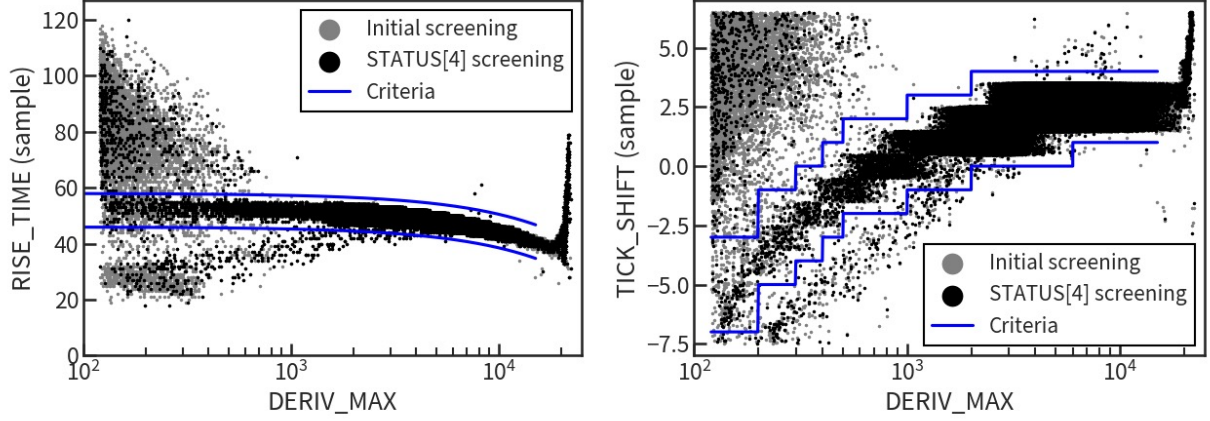


Fig 9 (left) `RISE_TIME` versus `DERIV_MAX` and (right) `TICK_SHIFT` versus `DERIV_MAX` distribution of Hp and Mp events using the in-orbit data of LMC X-3. The grey dots are events after the initial screening. The black dots are those after the additional screening to remove frame events. The value of `TICK_SHIFT` is dithered by ± 0.5 for presentation purposes. With the GV closed, events with an energy below ~ 1.7 keV cannot have originated from LMC X-3, but we expect real signal events to follow the trend shown here.

Table 3 Data sets used for the assessment of additional screening.

Label	Start time	Stop time	Exposure (ks)	Count rate ^a	Event threshold
GVO	2022/03/04 01:30	2022/03/09 23:00	403	3.2	75
Abell 2319	2023/10/14 07:25	2023/10/23 20:30	193	0.46	75
LMC X-3	2023/11/16 12:05	2023/11/17 13:50	204	0.49	120
	2023/11/30 08:04	2023/12/03 06:23			
NXB	2023/10/11 23:13	2023/10/31 19:50	650	0.43	75
	2023/10/31 19:50	2024/01/04 15:07			120

^a Counts rate of Hp and Mp grade events in 0.1–12 keV ($\text{s}^{-1} \text{pixel}^{-1}$)

a point source making a concentrated event distribution at the array center. We conducted spectral fitting of LMC X-3, the brightest of the two, and found that the X-ray signals below 1.7 keV is negligible, thus we use this energy as the boundary. The GVO data set was taken when the GV was open on the ground and provides data below ~ 1.7 keV, a region probed only by background events and spectral redistribution when the GV is closed.

We apply the additional screening and see how the background and signal events are affected. For signal events, we focus on the Hp and Mp grade events used for spectroscopy. Signal and background events dominate different energy bands for these data sets. Signal events dominate the whole band (0.1–20 keV) for the GVO data and in the science band (1.7–12 keV) for the two observations in the closed GV configuration. Background events dominate the whole band for the NXB data and in the soft band < 1.7 keV for the two observations.

Table 4 Ratio of the event rate after the additional screening to that before separately for the signal- or noise-dominant energy bands.

Label	Energy band (keV)	Ratio ^a
Signal-dominant band		
GVO	1.7–12	0.998
Abell 2319	1.7–12	0.95
LMC X-3	1.7–12	0.98
Noise-dominant band		
Abell 2319	0.1–1.7	0.05
LMC X-3	0.1–1.7	0.22
NXB	0.1–1.7	0.05

^a Ratio of the event rates after the additional screening to that before.

Table 4 shows the ratio of the event rate after screening to that before in the energy band where signal or noise events dominate. The reduced rate in the signal-dominant band is due either to the false coincidence or contamination of background events in the band. More events are removed by screening for the lowest count rate data set of Abell 2319 than for the other two sets. This is likely because background events are non-negligible in the signal-dominant band of the lowest count rate data set. Based on these data, we conclude that the percentage of real source data removed by the additional screening is less than 6%. For Abell 2319 and the NXB, the additional screening reduced the rate by $\sim 95\%$ below 1.7 keV. The reduction is lower for the highest count rate data set of LMC X-3. This is likely due to spectral redistribution from the signal dominant band at > 1.7 keV to the background dominant band at < 1.7 keV.²⁹ These redistributed events, resulting from phenomena such as the removal of energy by escaping photons or electrons after absorption of an x-ray, represent signal information, hence should not be removed as background but should be modeled through the redistribution matrix.

The resultant NXB spectrum after the additional screening is shown in Figure 8. The count rate is 1.0×10^{-3} counts s^{-1} keV $^{-1}$ in the 0.3–12 keV band, which is smaller than the requirement by a factor of 2. The additional screening is particularly useful below $\lesssim 2$ keV, which will be accessible after the GV opens in the orbit.

6 Conclusion

We presented the result of Resolve event screening using data acquired on the ground and in orbit. We assessed and optimized the screening criteria of individual screening items in three categories. New screening items (relative to SXS screening) for clipped events and ADR recycles were validated. More optimal screening criteria for the anti-coincidence detector, cross-talk events, and the SAA were developed. With the initial screening, we confirmed that the residual background rate is $1.8 \times 10^{-3} \text{ s}^{-1} \text{ keV}^{-1}$ in the 0.3–12.0 keV range to meet the requirement. With the additional screening based on the relationship between the pulse-shape properties characteristic of x-ray events, we found that the background is reduced further, in particular in the $\lesssim 2$ keV band, and becomes $1.0 \times 10^{-3} \text{ s}^{-1} \text{ keV}^{-1}$ in 0.3–12 keV. The additional screening will be particularly useful, when the GV is opened in the future, for soft diffuse extended sources such as supernova remnants. We will work to extend the bandpass beyond the requirement to allow access to the carbon features on the lower end and the Compton hump of many astrophysical objects on the high end. We expect refinements to the screening to be necessary. Currently, the multiple coincidence-based screening criteria overlap, and we are in the process of adding additional criteria to each, such as minimum and maximum ratios and size of the coincident group, such that the screening steps will be as distinct and precise as possible.

Acknowledgments

The substantial contributions of every member of the XRISM Resolve team enabled this work. We appreciate careful reading and useful comments for improvements by two anonymous reviewers. This work was supported by JSPS Core-to-Core Program (grant number:JPJSCCA20220002). This research has made use of data and software provided by the High Energy Astrophysics Science Archive Research Center (HEASARC), which is a service of the Astrophysics Science Division at NASA/GSFC. This work was supported by JST SPRING, Grant Number JPMJSP2108 and by Iwaware Scholarship Foundation in 2023. Part of this work was performed under the auspices of the U.S. Department of Energy by Lawrence Livermore National Laboratory under Contract DE-AC52-07NA27344. This paper is based on the SPIE proceeding.³⁶

DATA AVAILABILITY

The data that support the findings of this article are proprietary and are not publicly available. The data displayed in the figures above, as well as a limited subset of the underlying data, are available upon request at mochizuki@ac.jaxa.jp.

Disclosures

The authors declare there are no financial interests, commercial affiliations, or other potential conflicts of interest that have influenced the objectivity of this research or the writing of this paper.

References

- 1 M. S. Tashiro, S. Watanabe, H. Maejima, *et al.*, “Development and operation status of X-Ray Imaging and Spectroscopy Mission (XRISM),” in *Space Telescopes and Instrumentation 2024: Ultraviolet to Gamma Ray*, J.-W. A. Den Herder, K. Nakazawa, and S. Nikzad, Eds., 52, SPIE, (Yokohama, Japan) (2024).

- 2 Y. Ishisaki, R. L. Kelley, H. Awaki, *et al.*, “Status of resolve instrument onboard x-ray imaging and spectroscopy mission (XRISM),” in *Space Telescopes and Instrumentation 2022: Ultraviolet to Gamma Ray*, J.-W. A. Den Herder, K. Nakazawa, and S. Nikzad, Eds., 66, SPIE, (Montréal, Canada) (2022).
- 3 F. S. Porter, C. A. Kilbourne, M. Chiao, *et al.*, “In-flight performance of the XRISM/Resolve detector system,” *J. Astron. Telesc. Instrum. Syst.* **11** (2025).
- 4 F. S. Porter, G. V. Brown, K. R. Boyce, *et al.*, “The Astro-E2 X-ray spectrometer/EBIT microcalorimeter x-ray spectrometer,” *Review of Scientific Instruments*, Volume 75, Issue 10, pp. 3772-3774 (2004). **75**, 3772 (2004).
- 5 R. L. Kelley, K. Mitsuda, C. A. Allen, *et al.*, “The Suzaku High Resolution X-Ray Spectrometer,” *Publications of the Astronomical Society of Japan* **59**, 77–112 (2007).
- 6 R. L. Kelley, H. Akamatsu, P. Azzarello, *et al.*, “The Astro-H high resolution soft x-ray spectrometer,” *Society of Photo-Optical Instrumentation Engineers (SPIE) Conference Series* **9905**, 99050V (2016).
- 7 C. A. Kilbourne, M. Sawada, M. Tsujimoto, *et al.*, “In-flight calibration of Hitomi Soft X-ray Spectrometer. (1) Background,” *Publications of the Astronomical Society of Japan* **70** (2018).
- 8 C. A. Kilbourne, J. S. Adams, R. P. Brekosky, *et al.*, “Design, implementation, and performance of the Astro-H SXS calorimeter array and anticoincidence detector,” *Journal of Astronomical Telescopes, Instruments, and Systems* **4**, 1 (2018).
- 9 Hitomi Collaboration *et al.*, “Hitomi observations of the lmc snr n132d: Highly redshifted x-ray emission from iron ejecta,” *Publications of the Astronomical Society of Japan* **70**(2), 1–19 (2014).
- 10 M. Tsujimoto, K. Mitsuda, R. L. Kelley, *et al.*, “In-orbit operation of the soft x-ray spectrometer onboard the Hitomi satellite,” *Journal of Astronomical Telescopes, Instruments, and Systems* **4**, 1 (2017).
- 11 Y. Maeda, R. Fujimoto, H. Awaki, *et al.*, “Initial in-orbit operation of the soft x-ray spectrometer Resolve onboard the XRISM satellite,” *J. Astron. Telesc. Instrum. Syst.* **11** (2025).
- 12 M. E. Eckart, G. V. Brown, M. P. Chiao, *et al.*, “Energy gain scale calibration of the XRISM Resolve microcalorimeter spectrometer: Ground calibration results and on orbit comparison,” *J. Astron. Telesc. Instrum. Syst.* **11** (2025).
- 13 M. Mizumoto, M. Tsujimoto, R. Cumbee, *et al.*, “High count rate effects in event processing for XRISM/Resolve x-ray microcalorimeter,” *J. Astron. Telesc. Instrum. Syst.* **11** (2025).
- 14 M. E. Eckart, J. S. Adams, K. R. Boyce, *et al.*, “Ground calibration of the Astro-H (Hitomi) soft x-ray spectrometer,” *Journal of Astronomical Telescopes, Instruments, and Systems* **4**, 1 (2018).
- 15 T. Midooka, M. Tsujimoto, S. Kitamoto, *et al.*, “X-ray transmission calibration of the gate valve for the x-ray astronomy satellite XRISM,” *Journal of Astronomical Telescopes, Instruments, and Systems* **7**, 028005 (2021).
- 16 K. Sato, Y. Uchida, and K. Ishikawa, “Hitomi/XRISM micro-calorimeter,” (2023).
- 17 M. P. Chiao, J. S. Adams, P. A. Goodwin, *et al.*, “System design and implementation of the detector assembly of the Astro-H soft x-ray spectrometer,” *JATIS* **4**, 021404 (2018).
- 18 S. Eidelman, K. G. Hayes, K. A. Olive, *et al.*, “Review of Particle Physics,” *Physics Letters B* **592**, 1–5 (2004).

- 19 K. R. Boyce, M. D. Audley, R. G. Baker, *et al.*, “Design and performance of the ASTRO-E/XRS signal processing system,” in *EUV, X-Ray, and Gamma-Ray Instrumentation for Astronomy X*, **3765**, 741–750, SPIE (1999).
- 20 Y. Ishisaki, S. Yamada, H. Seta, *et al.*, “In-flight performance of pulse-processing system of the ASTRO-H/Hitomi soft x-ray spectrometer,” *Journal of Astronomical Telescopes, Instruments, and Systems* **4**, 011217 (2018).
- 21 M. Tsujimoto, M. S. Tashiro, Y. Ishisaki, *et al.*, “In-Orbit Performance of the Digital Electronics for the X-Ray Microcalorimeter Onboard the Hitomi Satellite,” *Journal of Low Temperature Physics* **193**, 505–511 (2018).
- 22 T. Omama, M. Tsujimoto, M. Sawada, *et al.*, “Relative timing calibration of the Resolve x-ray microcalorimeter onboard XRISM using the modulated x-ray source,” in *Space Telescopes and Instrumentation 2022: Ultraviolet to Gamma Ray*, J.-W. A. Den Herder, K. Nakazawa, and S. Nikzad, Eds., 267, SPIE, (Montréal, Canada) (2022).
- 23 Y. Terada, M. Holland, M. Loewenstein, *et al.*, “Detailed design of the science operations for the XRISM mission,” *Journal of Astronomical Telescopes, Instruments, and Systems* **7**, 037001 (2021).
- 24 T. F. Doyle, M. P. Holland, R. S. Hill, *et al.*, “The XRISM pipeline software system: Connecting continents, processes, testing, and scientists,” in *Space Telescopes and Instrumentation 2022: Ultraviolet to Gamma Ray*, **12181**, 1495–1506, SPIE (2022).
- 25 M. E. Eckart and Resolve Instrument team., “Resolve pulse clipping threshold,” *XRISM-RESOLVE-CALDB-CLIPTHR-219* (2024). Accessed 2024-09-18. Available at: https://heasarc.gsfc.nasa.gov/docs/xrism/calib/xrism_caldbdocs.html.
- 26 M. A. Leutenegger, M. E. Eckart, S. J. Moseley, *et al.*, “Simple, compact, high-resolution monochromatic x-ray source for characterization of x-ray calorimeter arrays,” *Review of Scientific Instruments* **91**, 083110 (2020).
- 27 P. J. Shirron, M. O. Kimball, R. S. Ottens, *et al.*, “On-orbit performance of the Adiabatic Demagnetization Refrigerator on XRISM,” *J. Astron. Telesc. Instrum. Syst.* **11** (2025).
- 28 M. J. DiPirro, P. J. Shirron, S. Yoshida, *et al.*, “Measuring the liquid helium volume on XRISM and predicting the liquid lifetime,” *J. Astron. Telesc. Instrum. Syst.* **11** (2025).
- 29 M. Tsujimoto, T. Okajima, M. E. Eckart, *et al.*, “In-flight Calibration of Hitomi Soft X-ray Spectrometer (3) Effective Area,” *Publications of the Astronomical Society of Japan* **70** (2018).
- 30 C. P. de Vries, D. Haas, N. Y. Yamasaki, *et al.*, “Calibration sources and filters of the soft x-ray spectrometer instrument on the Hitomi spacecraft,” *Journal of Astronomical Telescopes, Instruments, and Systems* **4**, 1 (2017).
- 31 R. F. Shipman, S. Kitamoto, R. Wolfs, *et al.*, “In-orbit operation of Resolve Filter Wheel and MXS,” *J. Astron. Telesc. Instrum. Syst.* **11** (2025).
- 32 M. Sawada, R. S. Cumbee, C. De Vries, *et al.*, “Strategies for the in-orbit gain tracking using the modulated x-ray sources for the Resolve microcalorimeter spectrometer on XRISM,” *J. Astron. Telesc. Instrum. Syst.* **11** (2025).
- 33 M. Sawada, R. S. Cumbee, C. P. De Vries, *et al.*, “Pulse parameters optimization of the modulated x-ray sources for the resolve microcalorimeter spectrometer on XRISM,” in *Space Telescopes and Instrumentation 2022: Ultraviolet to Gamma Ray*, J.-W. A. Den Herder, K. Nakazawa, and S. Nikzad, Eds., 269, SPIE, (Montréal, Canada) (2022).

- 34 L. Feretti, G. Giovannini, and H. Böhringer, “The radio and X-ray properties of Abell 2319,” *New Astronomy* **2**, 501–515 (1997).
- 35 A. P. Cowley, D. Crampton, J. B. Hutchings, *et al.*, “Discovery of a massive unseen star in LMC X-3,” *The Astrophysical Journal* **272**, 118–122 (1983).
- 36 Y. Mochizuki, M. Tsujimoto, C. A. Kilbourne, *et al.*, “Optimization of x-ray event screening using ground and in-orbit data for the Resolve instrument onboard the XRISM satellite,” in *Space Telescopes and Instrumentation 2024: Ultraviolet to Gamma Ray*, J.-W. A. Den Herder, K. Nakazawa, and S. Nikzad, Eds., 233, SPIE, (Yokohama, Japan) (2024).

Yuto Mochizuki is a graduate school student of The University of Tokyo and Institute of Space and Astronautical Science, Japan Aerospace Exploration Agency. He received his BS degree in physics from Tokyo University of Science and MS degree in astronomy from The University of Tokyo in 2022 and 2024, respectively. He is a student member of SPIE.

Biographies and photographs of the other authors are not available.

List of Figures

1	Conceptual example of the time derivative of an event.	5
2	Some examples of the pulse record of (a) normal events and events with (b) <code>QUICK_DOUBLE</code> , (c) <code>SLOPE_DIFFER</code> , (d) <code>FLAG_CLIPPED</code> , (e) short electrical crosstalk, and (f) frame event flags. Examples in (b)–(f) are not intended to be typical.	7
3	(a) Spectrum after initial screening with and without the <code>FLAG_CLIPPED</code> flag. (b) The energy resolution with and without events of <code>FLAG_CLIPPED</code> flag using the Y $K\alpha^1$ (15.0 keV), Mo $K\beta^1$ (19.6 keV), and Ag $K\alpha^1$ (22.2 keV) lines. The results are almost identical for the first two lines.	8
4	Arrival time of anti-co events relative to microcalorimeter events before (left) and after (right) the change of the event threshold on October 31, 2023. One sample time corresponds to 80 μ s. The offsets for the different event thresholds agree with each other in the range of errors because the use of correlation with the template eliminates dependence of the arrival time on threshold. different thresholds.	9
5	Result of short cross-talk assessment using the Au $L\alpha$ line data of individual pixels, arranged according to the physical layout of the pixels in the array, except for pixel 12 (calibration pixel). The distribution of arrival times of child events in pixel i relative to their parents in pixel $i + 1$ (top) and $i - 1$ (bottom). The child events in pixels $9n + 8$ ($n = 0, 1, 2, 3$) do not have parents in pixel $i + 1$ and child events in pixels $9n$ do not have parents in pixel $i - 1$ due to the boundaries of the readout line layout, which is confirmed with the data with a few false coincidence exceptions	10
6	Result of short cross-talk assessment using the Au $L\alpha$ line data of all pixels except for pixel 12 (calibration pixel); (left) arrival time of child event candidates relative to their parents and (right) ratio of the pulse height of child events against parents. We used Hp grade only both for the parent and child events.	11

7	(a) Map of anti-co count rate averaged over a 2×2 degree grid and red border defining SAA region (b) The NXB count rate (all event grades) of all pixels except for pixel 11, 12, and 13 (calibration pixel and its cross-talk neighbors). The rates in three different energy bands are shown in different colors. (c) The energy resolution in eV FWHM of the Mn $K\alpha$ line of pixel 12. Gray dash line in (b) and (c) shows the anti-co threshold used in the initial screening.	13
8	NXB spectra before any event screening (blue), initial screening (orange), and additional screening (green). Events of the Hp and Mp grade are used.	15
9	(left) RISE_TIME versus DERIV_MAX and (right) TICK_SHIFT versus DERIV_MAX distribution of Hp and Mp events using the in-orbit data of LMC X-3. The grey dots are events after the initial screening. The black dots are those after the additional screening to remove frame events. The value of TICK_SHIFT is dithered by ± 0.5 for presentation purposes. With the GV closed, events with an energy below ~ 1.7 keV cannot have originated from LMC X-3, but we expect real signal events to follow the trend shown here.	16

List of Tables

1	Resolve event screening items.	6
2	Data set used for the assessment of “short” cross-talk screening.	9
3	Data sets used for the assessment of additional screening.	16
4	Ratio of the event rate after the additional screening to that before separately for the signal- or noise-dominant energy bands.	17